Published by Avanti Publishers

The Global Environmental Engineers

ISSN (online): 2410-3624

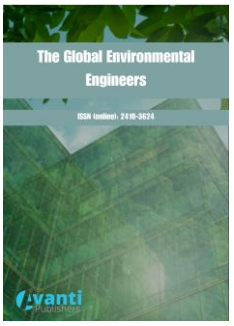

Oxidative Desulfurization of Model Fuel Using Ni or Mo-based Catalysts Supported on Bio-synthesized γ-Al_2O_3; Optimization of Synthesis Parameters

Sahar Miralaei Rad[1,2], Nader Rahemi[1,2,*], Somaiyeh Allahyari[1,2] and Pouria Akbari[1,2]

[1]*Chemical Engineering Faculty, Sahand University of Technology, Sahand New Town, Tabriz, Iran*

[2]*Environmental Engineering Research Centre, Sahand University of Technology, Sahand New Town, Tabriz, Iran*

ARTICLE INFO

Article Type: Research Article

Academic Editor: Nahed El Mahallawy

Keywords:
Ni
Mo
γ-Al_2O_3
Catalysis
Bio template
Oxidative desulfurization

Timeline:
Received: December 22, 2026
Accepted: February 16, 2026
Published: April 01, 2026

Citation: Rad SM, Rahemi N, Allahyari S, Akbari P. Oxidative desulfurization of model fuel using Ni or Mo-based catalysts supported on bio-synthesized γ-Al_2O_3; optimization of synthesis parameters. Glob Environ Eng. 2026; 13(1): 9-25.

DOI: https://doi.org/10.15377/2410-3624.2026.1.2

*Corresponding Author
Email: n_rahemi@sut.ac.ir
Tel: +(98) 41-33459100

ABSTRACT

In this study, γ-Al_2O_3 was synthesized via a green sol–gel route using four bio-templates (Pistacia Atlantica gum, glucose, gelatine, and gond katira gum) and applied as support for Ni- and Mo-based oxidative desulfurization (ODS) catalysts. XRD analysis confirmed the selective formation of high-purity γ-Al_2O_3 in all bio-templated samples, while gelatine-assisted alumina exhibited enhanced crystallinity. BET measurements revealed significantly increased surface areas (up to 190 $m^2 g^{-1}$) compared to non-templated alumina, and TEM analysis demonstrated uniform nanoparticles below 5 nm. Following metal deposition, FESEM and TEM analyses showed that ultrasound-assisted impregnation effectively reduced agglomeration and improved NiO dispersion over the mesoporous support. This structural refinement was further supported by BET results, which indicated improved accessible surface area in ultrasonically prepared catalysts compared with conventionally impregnated samples. The NiO/γ-Al_2O_3 catalyst prepared under ultrasound achieved 80% DBT conversion, outperforming conventionally impregnated NiO (76%), Mo-based catalyst (65%), and bare alumina (40%), highlighting the critical role of metal–support interaction and dispersion. A central composite design (CCD) approach was employed to optimize five synthesis and operational parameters (sol pH, calcination temperature, gelatine content, NiO loading, and oxidant-to-sulfur ratio). Under optimized conditions (pH 8.7, 685 °C calcination temperature, 3.65 wt.% gelatine, 16.86 wt.% NiO, O/S = 16.41), DBT conversion reached 98.11%, representing a substantial enhancement over the non-optimized ultrasonically prepared catalyst (80%). The optimized catalyst maintained high stability over seven consecutive cycles, with conversion decreasing only from 97.4% to 86.3%, and recovered to 91.5% after regeneration.

1. Introduction

Among various energy resources, fossil fuels remain the most accessible and widely utilized due to their high energy efficiency in industrial applications. However, their high sulfur content leads to severe environmental pollution and adverse health effects upon combustion. Therefore, stringent international environmental regulations have mandated a significant reduction in sulfur levels in transportation fuels, in some cases to below 10 ppm [1-3].

Hydrodesulfurization (HDS), the conventional industrial process for sulfur removal, is associated with high energy consumption, elevated hydrogen demand, and substantial capital investment [4-6]. Moreover, refractory aromatic sulfur compounds such as dibenzothiophene (DBT), 4-methyldibenzothiophene (4-MDBT), and 4,6-dimethyldibenzothiophene (4,6-DMDBT) are resistant to HDS due to steric hindrance and high electron density around the sulfur atom [7, 8]. To achieve deeper desulfurization, complementary techniques including adsorption desulfurization (ADS), extractive desulfurization (EDS), biodesulfurization (BDS), and oxidative desulfurization (ODS) have been explored. Among these, ODS has attracted considerable attention owing to its high efficiency, operational simplicity, and mild reaction conditions without the need for hydrogen [9-11]. The ODS process generally involves two main steps. First, sulfur-containing compounds are selectively oxidized to their corresponding sulfoxides and sulfones in the presence of a suitable oxidant and catalyst. Subsequently, the oxidized products are removed from the fuel phase using a polar extraction solvent [12]. The selection of an appropriate oxidant and the rational design of an efficient catalyst are therefore critical factors in ODS performance.

Heterogeneous supported catalysts, particularly those containing transition-metal oxides as active phases, have shown promising activity in ODS systems [13, 14]. Various mesoporous materials have been investigated as catalyst supports, including silica [15, 16], alumina [17], titania [18-20], mixed oxides [21, 22], zeolites [23], and metal–organic frameworks (MOFs) [24, 25].

γ-Al_2O_3 (activated alumina) is one of the most widely used supports due to its high specific surface area, excellent adsorption capacity, thermal stability, and abundant Lewis acid sites. These Lewis sites facilitate the adsorption of sulfur compounds through coordination between the lone pair electrons of sulfur and the vacant orbitals of aluminum atoms [26].

Recently, biosynthesis approaches for alumina preparation have gained increasing attention as environmentally friendly alternatives [27-29]. In such methods, natural bio-templates such as humin [30], eggshell membrane [31], yeast cells [32], and eggplant peel [33] have been employed to reduce the use of toxic reagents and promote sustainable synthesis routes.

In the present study, γ-alumina was synthesized using various bio-additives, including wild Pistacia Atlantica tree gum, glucose, gelatin, and gond katira gum, and subsequently employed as a support for NiO and MoO_3 in the oxidative desulfurization of a model fuel. To the best of our knowledge, these specific bio-templates have not previously been investigated for alumina synthesis, nor has bio-templated alumina been systematically applied as a support in ODS processes. Furthermore, Design-Expert software was utilized to optimize the synthesis parameters and enhance catalyst performance.

2. Materials and Methods

2.1. Materials

Sodium aluminate (98 wt% $Na_2O{\cdot}Al_2O_3$, FAMCO, Iran) was used as the alumina precursor. Distilled water and absolute ethanol (≥99.8%, analytical grade) were used as solvents. Hydrochloric acid (37 wt% HCl, analytical grade, Merck, Germany) was used for pH adjustment. Pistacia Atlantica gum and gond katira gum (collected from Zagros Mountains, southwestern Iran, dried and powdered before use), glucose (≥99%, analytical grade), and gelatin (food grade, Farmand company, Iran) were used as bio-templates. Nickel nitrate hexahydrate (97%, $Ni(NO_3)_2{\cdot}6H_2O$, Merck, Germany) was used as the nickel precursor. Natural molybdenite (MoS_2, Sungun mine, East Azerbaijan,

Iran, ground and sieved to <100 mesh prior to use) was used as the molybdenum source. Dibenzothiophene (98%, Merck, Germany) was used as the model sulfur compound. Acetonitrile (≥99.9%, HPLC grade, Sigma-Aldrich, USA) was used as the extraction solvent. n-Hexane (≥99%, Dr Mojallali, Iran) was used as model fuel. Hydrogen peroxide (30 wt%, Ghatranshimi, Iran) was used as oxidant in oxidative desulfurization experiments.

2.2. Nanocatalyst Preparation

2.2.1. Bio Template-assisted Synthesis of γ-alumina

Alumina powder was synthesized via a green sol–gel method according to our previous report [34]. Initially, a predetermined amount of sodium aluminate was dissolved in distilled water under continuous stirring. Separately, the bio-template was dissolved in ethanol and subsequently added dropwise to the sodium aluminate solution under vigorous stirring to obtain a homogeneous and transparent sol.

Hydrochloric acid was then gradually introduced to adjust the pH and promote gel formation. The resulting gel was aged at 90 °C for 3 h in an oven. After aging, the gel was washed three times with hot distilled water to remove residual ions and impurities, followed by drying at 120 °C overnight. Finally, the dried material was calcined at 700 °C for 5 h to obtain γ-Al_2O_3 [35].

The same procedure was employed using different bio-templates. The synthesized samples were denoted as $PGAl_2O_3$(SG), $GlAl_2O_3$(SG), $GeAl_2O_3$(SG), and $GKAl_2O_3$(SG), corresponding to Pistacia Atlantica gum, glucose, gelatin, and gond katira gum, respectively. The alumina sample prepared without any bio-template was designated as Al_2O_3(SG).

2.2.2. Synthesis of MoO_3/Al_2O_3 and NiO/OAl_2O_3 Catalysts

Impregnation Method

Molybdenite was impregnated onto the biosynthesized alumina support and the resulting sample was denoted as Mo/Al_2O_3(ISG). In a typical procedure, molybdenite powder was dispersed in the alumina slurry and the suspension was stirred at 60 °C for 3 h to ensure uniform distribution of the active phase. The obtained material was then dried at 110 °C for 24 h and subsequently calcined in air at 600 °C for 5 h [36], leading to the formation of MoO_3 species supported on Al_2O_3.

Similarly, Ni/Al_2O_3(ISG) refers to the catalyst prepared via conventional impregnation of nickel precursor onto the biosynthesized alumina support, followed by drying and calcination under identical conditions, resulting in NiO as the active phase.

Ultrasonic-assisted Impregnation Method

For the ultrasonic-assisted synthesis, an appropriate amount of nickel nitrate was mixed with alumina to form a homogeneous suspension, which was then subjected to ultrasonic irradiation for 30 min to enhance dispersion of the precursor. The resulting material was dried at 110 °C for 24 h and calcined in air at 600 °C for 5 h. The final catalyst was denoted as Ni/Al_2O_3(USG). The overall preparation procedure of the synthesized samples is illustrated in Fig. (**1**).

2.3. Characterization of Catalyst

X-ray diffraction (XRD) patterns were recorded using a Siemens D5000 X-ray diffractometer over a 2θ range of 10–80° to determine the crystalline phases of the samples. The morphology and surface structure were examined by field-emission scanning electron microscopy (FESEM, TESCAN BRNO Mira3 LMU). The specific surface area and textural properties were determined by N_2 adsorption–desorption measurements using the Brunauer–Emmett–Teller (BET) method on a Quantachrome ChemBET-3000 analyzer. Fourier transform infrared (FTIR) spectra were recorded on a TENSOR 27 spectrometer to identify surface functional groups. Transmission electron microscopy (TEM, Philips EM 208S) equipped with energy-dispersive X-ray spectroscopy (EDX) was employed to investigate the microstructure and elemental composition of the catalysts.

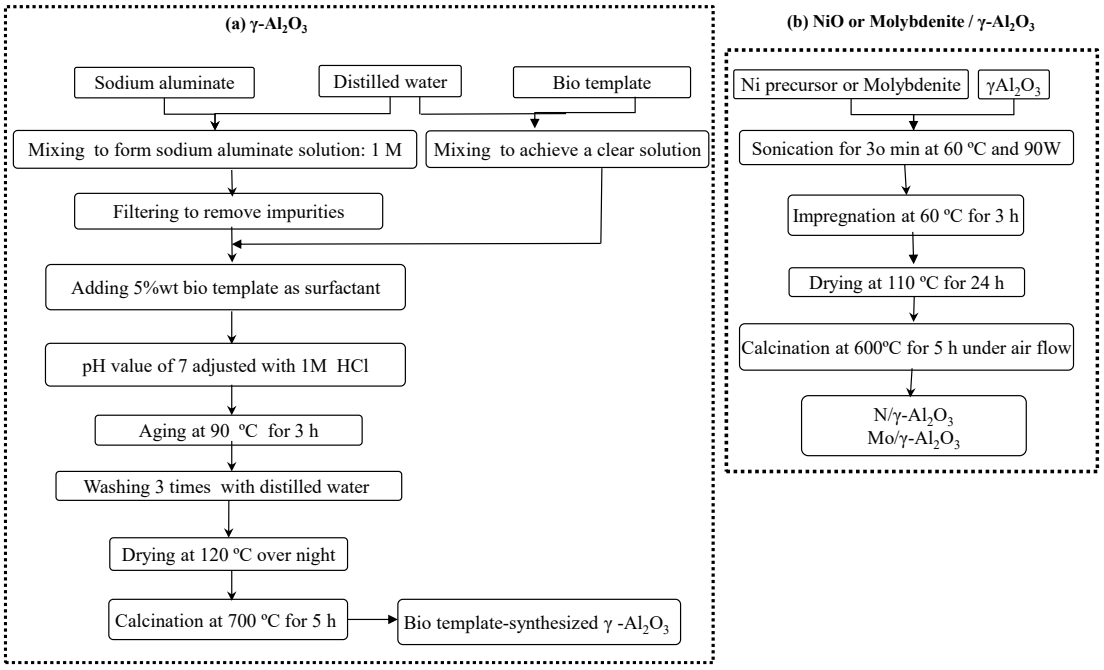

Figure 1: Schematic flow chart for the preparation steps of bio template assisted synthesis of γ-Al_2O_3 and NiO or MoO_3/γ-Al_2O_3.

2.4. Oxidative Desulfurization

As illustrated in Fig. (**2**), the model fuel was prepared by dissolving dibenzothiophene (DBT) in n-hexane to obtain a sulfur concentration of 500 ppm. In a typical oxidative desulfurization (ODS) experiment, 50 mL of model fuel, 1 mL of hydrogen peroxide (H_2O_2) as oxidant, and 0.2 g of catalyst were introduced into a round-bottom flask and stirred in a thermostatically controlled water bath at 60 °C. The reaction was allowed to proceed for 60 min under continuous stirring. After completion of the reaction, the mixture was transferred to a separatory funnel, and an equal volume of acetonitrile was added to extract the oxidized sulfur compounds. The extraction process was repeated four times to ensure maximum removal of the oxidized products. The residual DBT concentration in the fuel phase was determined using UV–Vis spectrophotometry.

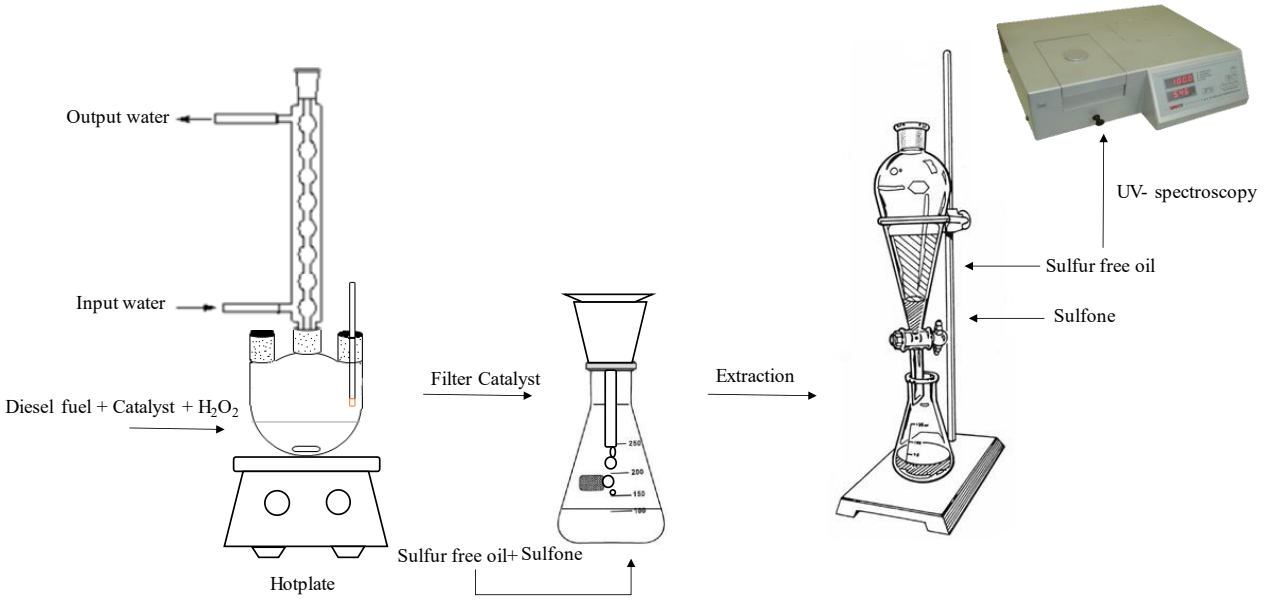

Figure 2: Experimental setup of oxidative desulfurization using synthesized catalysts.

3. Results and Discussions

3.1. Characterization of Bio-synthesized γ-Al_2O_3

3.1.1. XRD Analysis

Fig. (**3**) presents the XRD patterns of alumina synthesized without any bio-template (Al_2O_3(SG)) and those synthesized using various bio-templates: PGAl_2O_3(SG), GlAl_2O_3(SG), GeAl_2O_3(SG), and GKAl_2O_3(SG). Analysis of the diffraction patterns using JCPDS cards revealed that, in the absence of a bio-template, the alumina precursor was converted to corundum (rhombohedral phase, JCPDS card 01-077-2135). In contrast, all bio-template-assisted syntheses, irrespective of the template type, yielded γ-alumina (JCPDS card 01-001-1303).

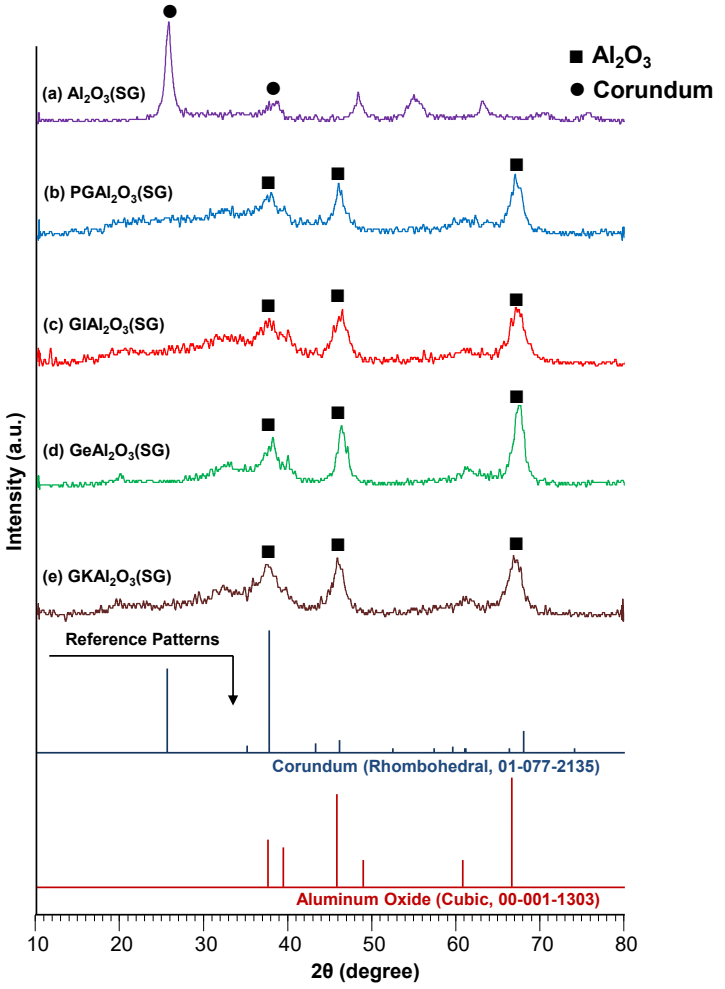

Figure 3: XRD patterns of bio template synthesized alumina: **a**) without bio template (Al_2O_3(SG)), **b**) with pistacia atlantica gum (PGAl_2O_3(SG)), **c**) with glucose (GeAl_2O_3(SG)), **d**) with gelatine (GlAl_2O_3(SG)), and **e**) with gond katira gum (GKAl_2O_3(SG)).

No additional diffraction peaks were observed in any of the bio-templated samples, indicating that high-purity γ-alumina was obtained [35]. Although all samples exhibited relatively low crystallinity, the intensity of the diffraction peaks in GeAl_2O_3(SG) was higher than in the other samples, suggesting that this sample possesses comparatively greater crystallinity. The higher crystallinity observed for GeAl_2O_3(SG) compared with other bio-templated samples can be attributed to the unique physicochemical properties of gelatin. Gelatin is a protein-based biopolymer containing amino (–NH_2), carboxyl (–COOH), and amide (–CONH–) functional groups, which can coordinate with Al^{3+} species during sol formation. This coordination promotes a more homogeneous distribution of aluminum centers within the organic–inorganic hybrid network and enables controlled nucleation during gelation. Moreover, the gradual thermal decomposition of gelatin during calcination may provide a more uniform structural evolution, facilitating the formation of well-defined γ-Al_2O_3 crystallites. In contrast, polysaccharide-

based templates such as glucose and plant gums mainly provide hydroxyl functionalities with comparatively weaker coordination ability and different decomposition behavior, which may lead to less controlled crystallization and consequently lower crystallinity.

3.1.2. BET Analysis

Fig. (**4**) presents the BET surface areas of Al_2O_3(SG), $PGAl_2O_3$(SG), $GlAl_2O_3$(SG), $GeAl_2O_3$(SG), and $GKAl_2O_3$(SG). Among the studied samples, Al_2O_3(SG) exhibited the lowest surface area of 112 m²/g. In contrast, alumina samples synthesized using bio-templates, including $GlAl_2O_3$(SG), $GeAl_2O_3$(SG), and $GKAl_2O_3$(SG), displayed significantly higher surface areas, approximately twice that of commercial γ-alumina (~104 m²/g). This enhancement highlights the positive role of bio-templates in structuring the alumina network during synthesis. Notably, glucose-assisted alumina ($GlAl_2O_3$(SG)) achieved the highest surface area of 195 m²/g.

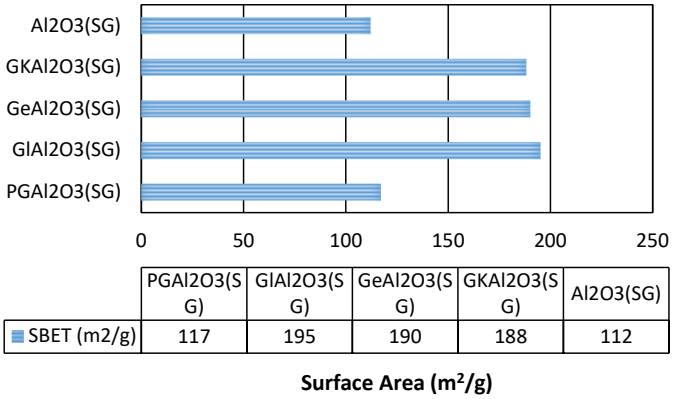

Figure 4: BET surface area of $PGAl_2O_3$(SG), $GeAl_2O_3$(SG), $GlAl_2O_3$(SG), and $GKAl_2O_3$(SG).

3.1.3. TEM and EDX Analyses

$GeAl_2O_3$(SG) was selected for further studies owing to its higher crystallinity and relatively high surface area. TEM analysis revealed that this sample consists of fine and uniformly distributed alumina particles. The particle size was determined to be below 5 nm, which is consistent with the observed high surface area. Additionally, EDX analysis performed on the TEM images confirmed the presence of aluminum and oxygen, verifying the composition of the sample (Fig. **5**).

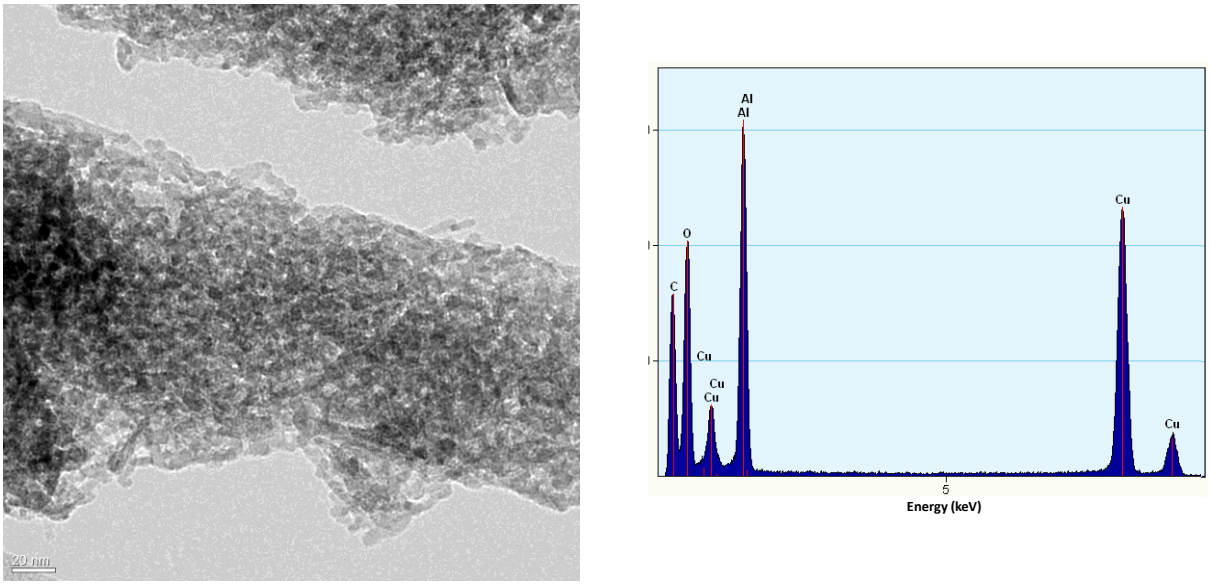

Figure 5: TEM and EDX analysis of $GeAl_2O_3$(SG).

3.2. Characterization of $Ni/GeAl_2O_3$ and $Mo/GeAl_2O_3$; Effect of Active Phase and Synthesis Method

Owing to the high surface area and relatively high crystallinity of gelatin-synthesized alumina, NiO and MoO_3 were deposited on this support via conventional impregnation or ultrasonic-assisted methods. The influence of the active phase and the synthesis technique on catalyst properties and performance is discussed in this section.

3.2.1. FESEM Analysis

The FESEM images of $GeAl_2O_3$(SG), $Mo/GeAl_2O_3$(ISG), $Ni/GeAl_2O_3$(ISG), and $Ni/GeAl_2O_3$(USG) are shown in Fig. (**6**). As illustrated in Fig. (**6a**), $GeAl_2O_3$(SG) consists of fine spherical particles forming agglomerates of 5–50 nm. Fig. (**6b**) shows MoO_3, derived from a molybdenite source and impregnated on gelatine-assisted synthesized alumina ($Mo/GeAl_2O_3$(ISG)), exhibiting very uniform, small 0D particles. However, these extremely fine nanoparticles tend to aggregate severely due to their high surface energy [37].

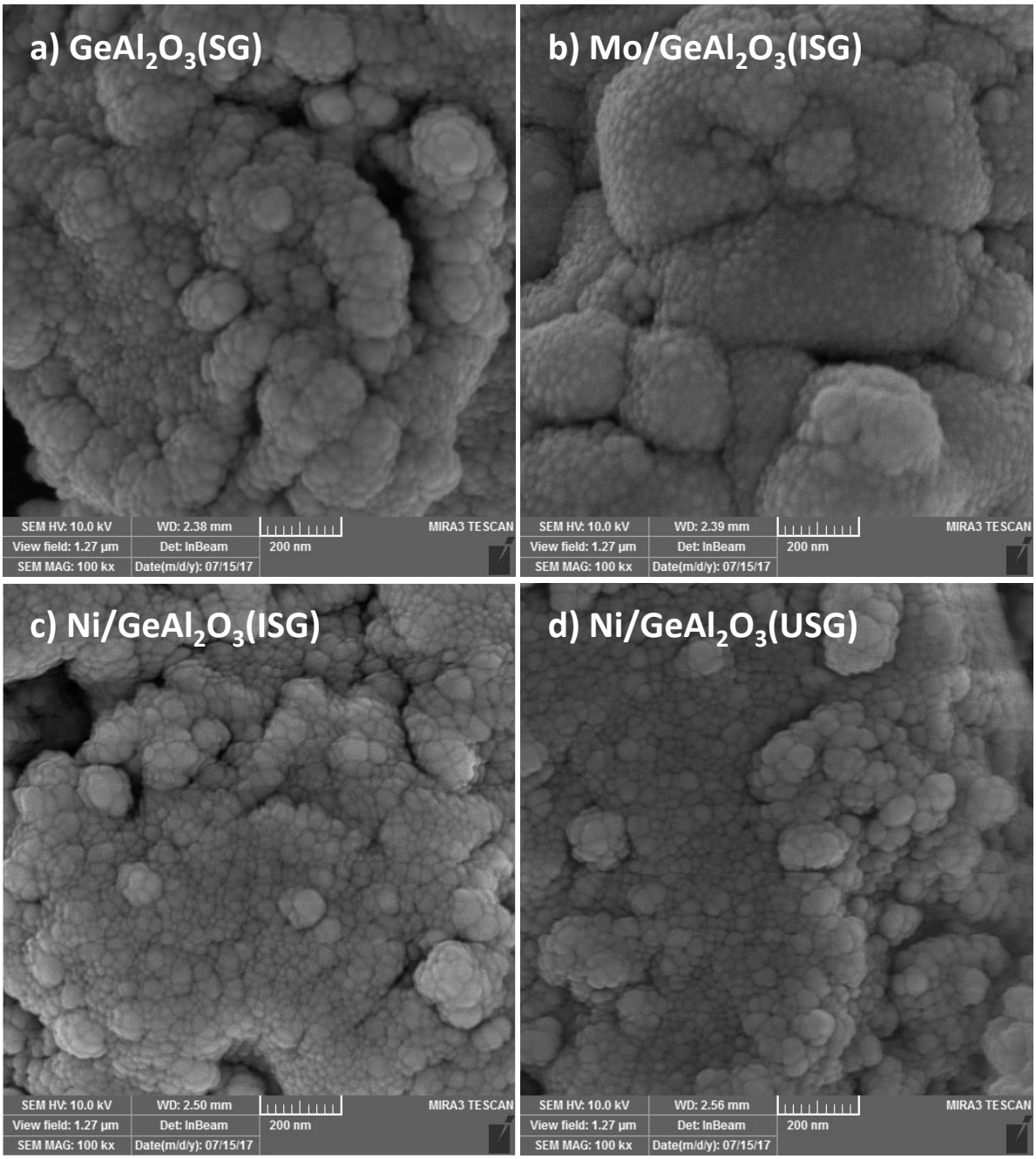

Figure 6: FESEM images of (a) $GeAl_2O_3$(SG), (b) $Mo/GeAl_2O_3$(ISG), (c) $Ni/GeAl_2O_3$(ISG), and (d) $Ni/GeAl_2O_3$(USG).

Literature on Mo/Al_2O_3 systems indicates that the strength of Mo–support interactions critically influences dispersion and agglomeration. Strong Mo–O–Al linkages (e.g., via polymolybdate anchoring on defect sites or hydroxyl groups of γ-alumina) promote better initial dispersion and enhance resistance to agglomeration during calcination. In contrast, weaker interactions result in mobile Mo species, leading to the severe agglomeration observed in this sample.

Fig. (**6c**) depicts NiO impregnated on alumina ($Ni/GeAl_2O_3$(ISG)), showing widely distributed, agglomerated nanoparticles. Fig. (**6c**) and (**6d**) compare the effect of sonication during NiO deposition on $GeAl_2O_3$(SG). Sonication fractures agglomerates and produces a smoother, more uniform morphology, which enhances NiO–alumina interactions—an important factor for oxidative desulfurization (ODS) catalysts [17].

Ultrasound promotes acoustic cavitation, where microbubbles form, grow, and collapse asymmetrically near the γ-Al_2O_3 surface. The collapse generates high-velocity microjets (~100–200 m/s) and intense shock waves, which improve NiO dispersion and anchoring via several mechanisms. First, microjets disrupt boundary layers around alumina particles, allowing uniform penetration of Ni^{2+} precursor species into pores and across surfaces, reducing local oversaturation and preventing agglomeration. Second, shear forces and shock waves remove surface impurities, expose defect sites, and increase hydroxyl group density, providing more reactive anchoring points for Ni species. Third, transient high temperatures and pressures promote heterogeneous nucleation on the support surface rather than in the bulk solution, yielding smaller, more uniform $Ni(OH)_2$ or NiO_x nuclei. Additionally, microjets fragment growing clusters, further limiting particle size. Finally, the direct impact of microjets strengthens physical adsorption and chemical interactions (e.g., Ni–O–Al linkages) between nickel nuclei and the alumina surface, enhancing resistance to sintering during calcination.

3.2.2. EDX Analysis

Although EDX provides primarily surface-localized information, it can still offer insights into elemental distribution. Fig. (**7a**) shows the gelatine-synthesized alumina. The presence of Na and Cl indicates incomplete washing and residual sodium chloride byproduct in the sample. The Au peaks observed in all samples arise from gold coating applied to improve conductivity during EDX analysis.

In Fig. (**7b**), the intensity of Al peaks decreases in $Mo/GeAl_2O_3$(ISG), reflecting surface coverage by Mo and S species. Comparison of Fig. (**7c**) and (**7d**) shows that while Ni-related peaks are similar in both samples, the sonicated sample exhibits sharper and more intense Al and O peaks. This indicates that sonication fractures alumina agglomerates, exposing more alumina surface and enhancing interactions between the active Ni phase and the support.

3.2.3. BET Analysis

Fig. (**8**) shows that the specific surface area of gelatine-synthesized alumina (190 m^2/g) decreases upon introduction of the active phase, a common trend in supported catalysts [38] caused by pore blockage during impregnation. $Mo/GeAl_2O_3$(ISG) exhibits the lowest surface area (53.6 m^2/g), which FESEM attributes to strong agglomeration in this catalyst. In contrast, $Ni/GeAl_2O_3$(ISG) shows a more open morphology and correspondingly higher surface area, consistent with FESEM observations. The application of ultrasound during synthesis further increases the BET surface area of $Ni/GeAl_2O_3$(USG) to 125.6 m^2/g, the highest among the supported catalysts. Ultrasound-induced microjets break up agglomerates, enlarging the exposed surface and enhancing accessibility of the active phase for reactions such as oxidative desulfurization (ODS) [39-42].

3.2.4. FTIR Analysis

The FTIR spectra of the synthesized catalysts ($GeAl_2O_3$(SG), $Mo/GeAl_2O_3$(ISG), $Ni/GeAl_2O_3$(ISG), and $Ni/GeAl_2O_3$(USG)) are shown in Fig. (**9**). The bands at 590 and 750 cm^{-1} correspond to Al–O–Al bending and Al–O stretching vibrations, respectively, characteristic of alumina [43], and are observed in all samples. Sharp peaks between 1500 and 1700 cm^{-1} are attributed to $Al(OH)_3$, likely due to the relatively low calcination temperature [44]. The Ni–O vibration below 500 cm^{-1} was not detected due to the FTIR instrument's range.

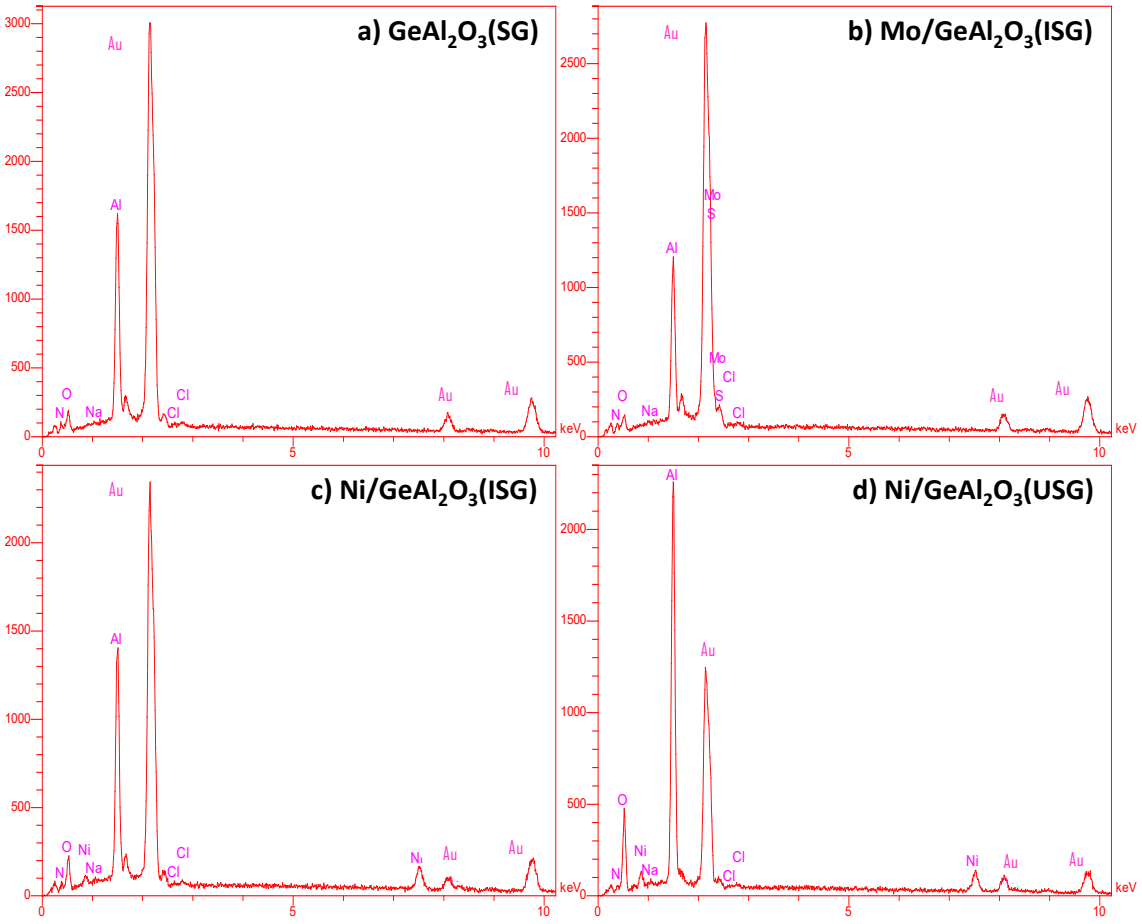

Figure 7: EDX analysis of (a) $GeAl_2O_3$(SG), (b) Mo/$GeAl_2O_3$(ISG), (c) Ni/$GeAl_2O_3$(ISG), and (d) Ni/$GeAl_2O_3$(USG).

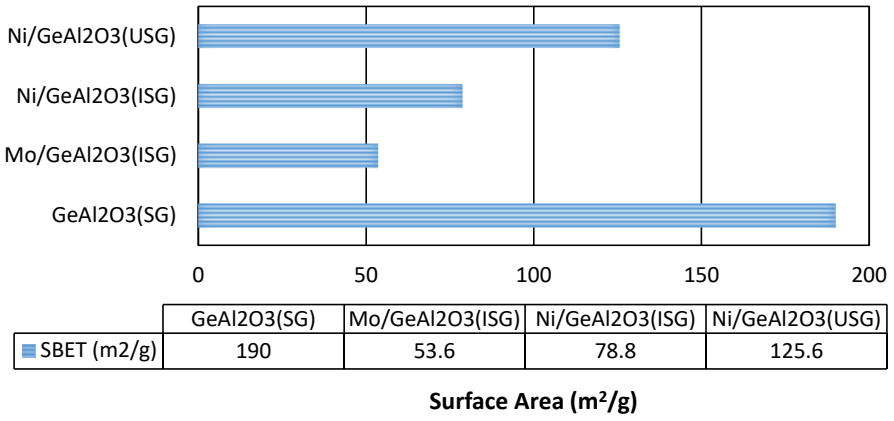

Figure 8: BET surface area of $GeAl_2O_3$(SG), Mo/$GeAl_2O_3$(ISG), Ni/$GeAl_2O_3$(ISG), and Ni/$GeAl_2O_3$(USG).

In Mo/$GeAl_2O_3$(ISG), the band at 560-1000 cm^{-1} are assigned to Mo–O in MoO_3 [45]. Peaks at 1650 and 3450 cm^{-1} correspond to adsorbed water, with intensities correlating with BET surface area—samples with higher surface area adsorb more water [46]. Additionally, $Al(OH)_3$ gives rise to bands between 3700 and 3850 cm^{-1} in all samples [47].

3.2.5. TEM and EDX Analysis

The morphology and elemental composition of Ni/$GeAl_2O_3$(USG) are shown in Fig. (**10**). Fine $GeAl_2O_3$ particles exhibit small, uniform spherical shapes (<5 nm), while NiO particles are well-dispersed with larger sizes (20–30

nm). The uniform dispersion of NiO is attributed to ultrasound-assisted impregnation, which enhances interactions between the active NiO phase and the alumina support—a critical factor in ODS catalysis. EDX analysis confirms the presence of Ni, Al, and O in the sample. The improved dispersion observed in FESEM and TEM images corresponds with BET results, showing increased accessible surface area and reduced pore blockage. These observations are consistent with literature on ultrasound-assisted improved dispersion of metal oxide in supported catalysts [39, 40].

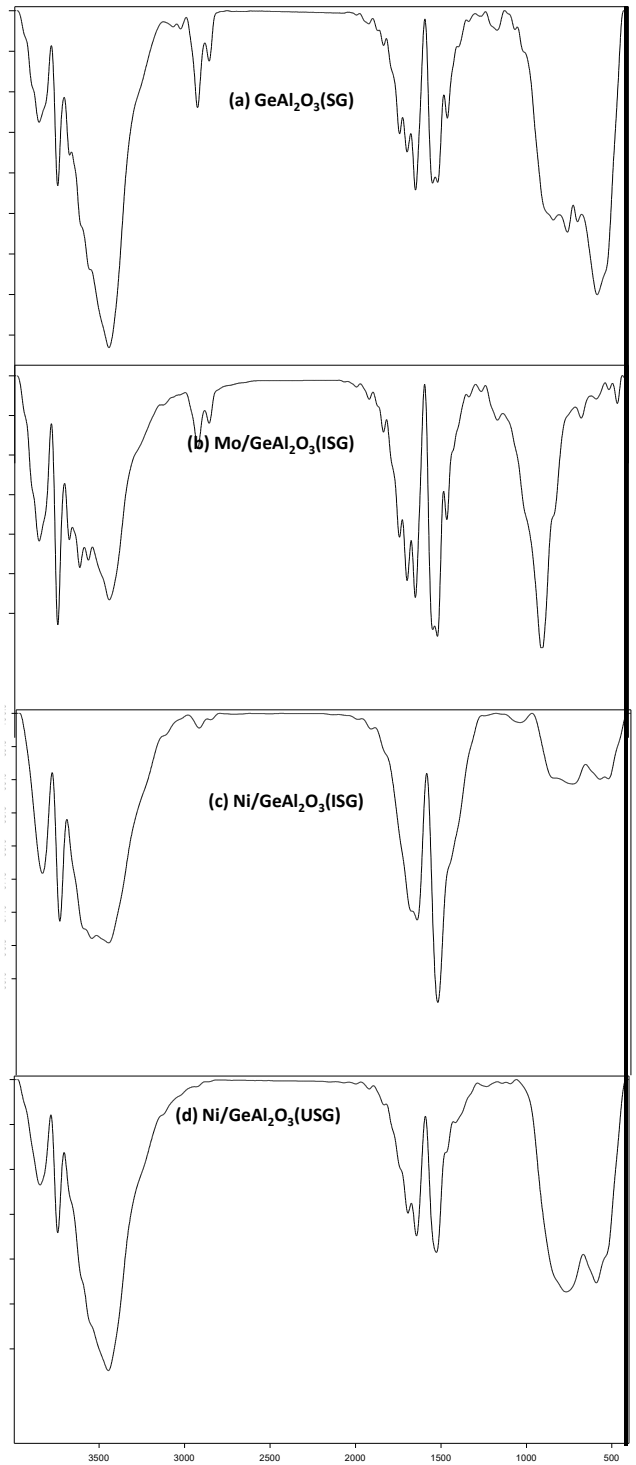

Figure 9: FTIR spectra of $GeAl_2O_3$(SG), Mo/$GeAl_2O_3$(ISG), Ni/$GeAl_2O_3$(ISG), and Ni/$GeAl_2O_3$(USG). Ni/$GeAl_2O_3$(USG), Ni/$TGAl_2O_3$(USG)).

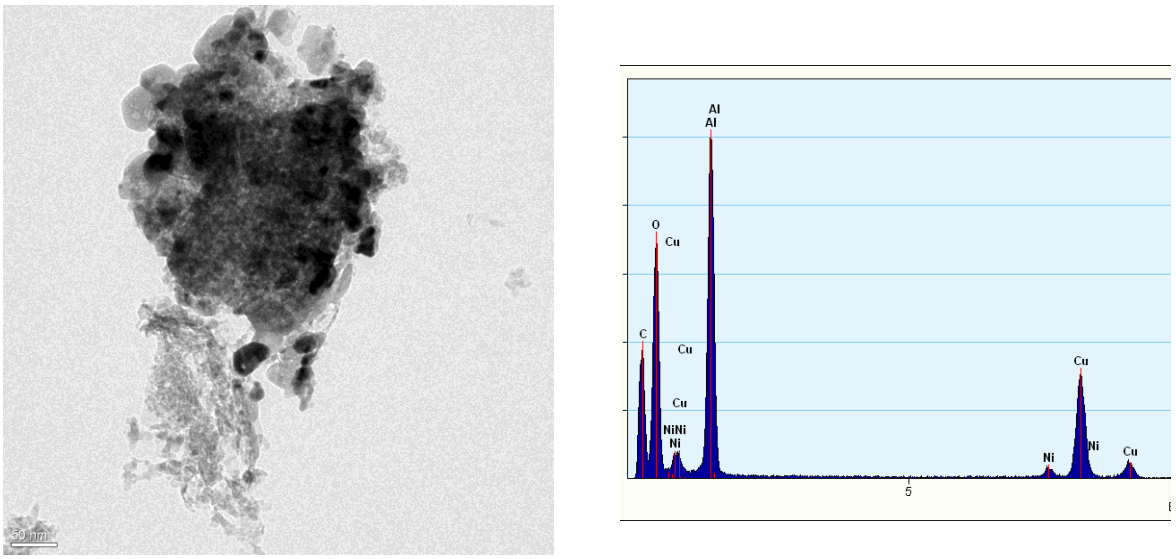

Figure 10: TEM and EDX analysis of Ni/$GeAl_2O_3$(USG).

3.3. Ni/$GeAl_2O_3$(USG) Performance in ODS

$GeAl_2O_3$(SG), Mo/$GeAl_2O_3$(ISG), Ni/$GeAl_2O_3$(ISG), and Ni/$GeAl_2O_3$(USG) were tested for DBT desulfurization from n-hexane as a model fuel (Fig. **11**). In the blank test (without catalyst, using only H_2O_2), only 36% of DBT was degraded, indicating that hydroxyl radicals from H_2O_2 decomposition alone provide limited oxidation and highlighting the necessity of a catalyst. Gelatine-synthesized alumina increased DBT degradation slightly to 40%. Incorporation of MoO_3 and NiO on the bio-synthesized alumina significantly improved activity, with Ni/$GeAl_2O_3$(USG) achieving the highest DBT conversion of 80%. This enhanced performance is attributed to the synergy between NiO and alumina, high NiO dispersion with uniform morphology on highly porous alumina due to sonication, strong NiO–alumina interactions, and the large surface area of the catalyst. Nevertheless, DBT conversion is not yet optimal, and further improvements are expected by optimizing synthesis conditions and reaction parameters.

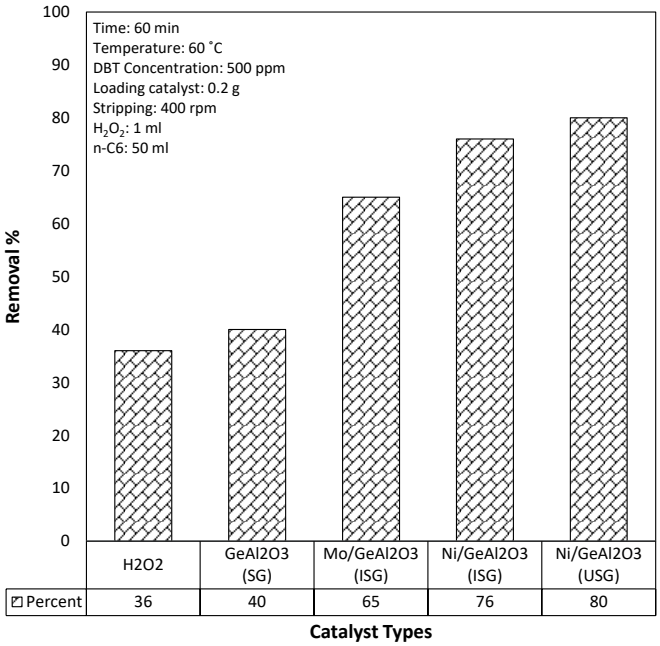

Figure 11: DBT oxidation without catalyst (just H_2O_2), catalysed by $GeAl_2O_3$(SG), Mo/$GeAl_2O_3$(ISG), Ni/$GeAl_2O_3$(ISG), Ni/$GeAl_2O_3$(USG). Reaction condition; temperature 60˚C, time 60 minutes, catalyst 0.2g, fuel 50ml and DBT concentration 500ppm.

3.4. Optimization of the Synthesis and Operational Parameters

For the remainder of the study, Ni/$GeAl_2O_3$(USG) was selected, and Design Expert was employed to optimize both structural and operational parameters. Four structural factors—pH of the parent sol, calcination temperature, weight percent of gelatine, and weight percent of NiO—and one operational factor, the oxidant-to-DBT molar ratio (O/S), were investigated to maximize DBT conversion. The experimental matrix was generated using the CCD method, comprising 32 experiments. All reactions were conducted under consistent conditions: catalyst loading of 0.2 g, DBT concentration of 500 ppm, temperature of 60 °C, and reaction time of 60 minutes.

3.4.1. Effect of Alumina Sol pH

simultaneous effect of alumina sol pH and O/S ratio and NiO weight percent were studied in Fig. (**12**). Fig. (**12a**) and (**12b**) show increasing the pH in both cases enhances the catalyst activity. Fig. (**12a**) confirmed that by adjusting the alumina sol pH in alkaline conditions, even at low NiO wt.%, a catalyst with high ODS activity would be synthesized. This is important from an economical point of view because catalyst cost is mainly dictated by the active phase content. Fig. (**12b**) indicated the higher impact of pH as a synthesis parameter compared to O/S as an operating parameter on the activity of the catalyst. This means with a well-designed catalyst, the need for harsh operating conditions lowers.

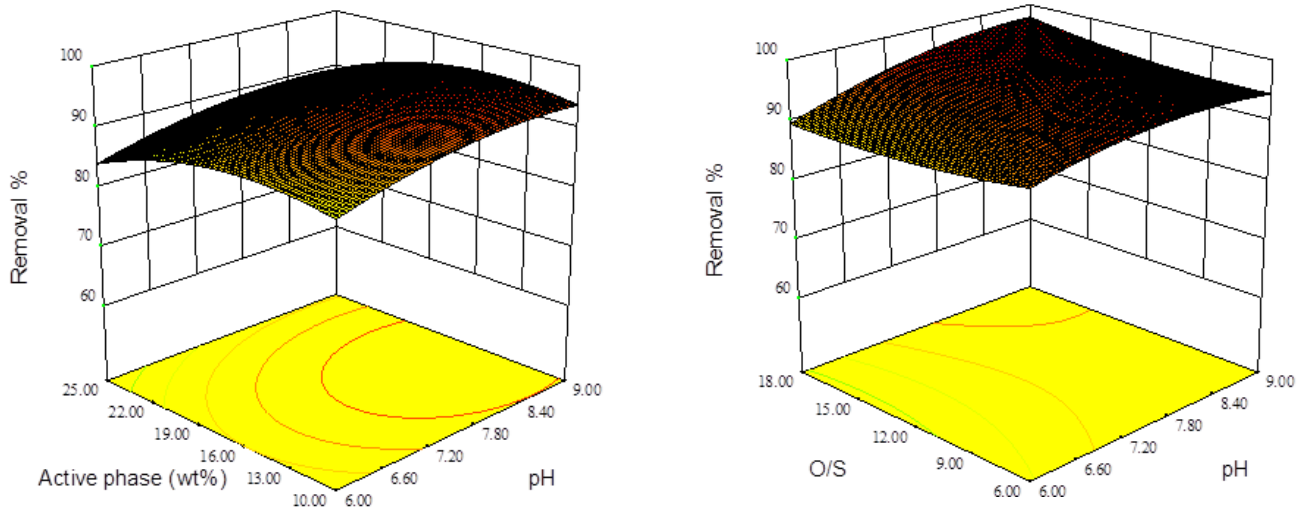

a) Effect of alumina sol pH pH and NiO %wt.

b) Effect of alumina sol pH and O/S.

Figure 12: 3-D diagram of the effect of pH, NiO wt.% and O/S on the removal efficiency of DBT in the ODS process. Reaction condition: temperature 60˚C, time 60 minutes, catalyst 0.2g, fuel 50 ml and DBT concentration 500 ppm.

3.4.2. Effect of Gelatine Content

As shown in Fig. (**13a**), increasing the NiO content from 10 to 17.5 wt.% enhances catalyst activity, even at low gelatine levels. However, further increasing NiO to 25 wt.% reduces activity, which can be partially compensated by higher gelatine content. Fig. (**13b**) highlights the stronger influence of pH compared to gelatine. At low gelatine levels, increasing pH improves catalyst activity, while at acidic pH, higher gelatine content enhances performance. The maximum activity is achieved at high pH and moderate gelatine content.

3.4.3. Effect of NiO Content

In Fig. (**14**), the 3-D diagram shows the effect of the active phase along with the O/S ratio and calcination temperature. It is observed that a higher O/S ratio in both low and high NiO contents would increase the catalyst activity. Fig. (**14b**) shows that moderate calcination temperature and moderate NiO weight percent yield the highest DBT conversion.

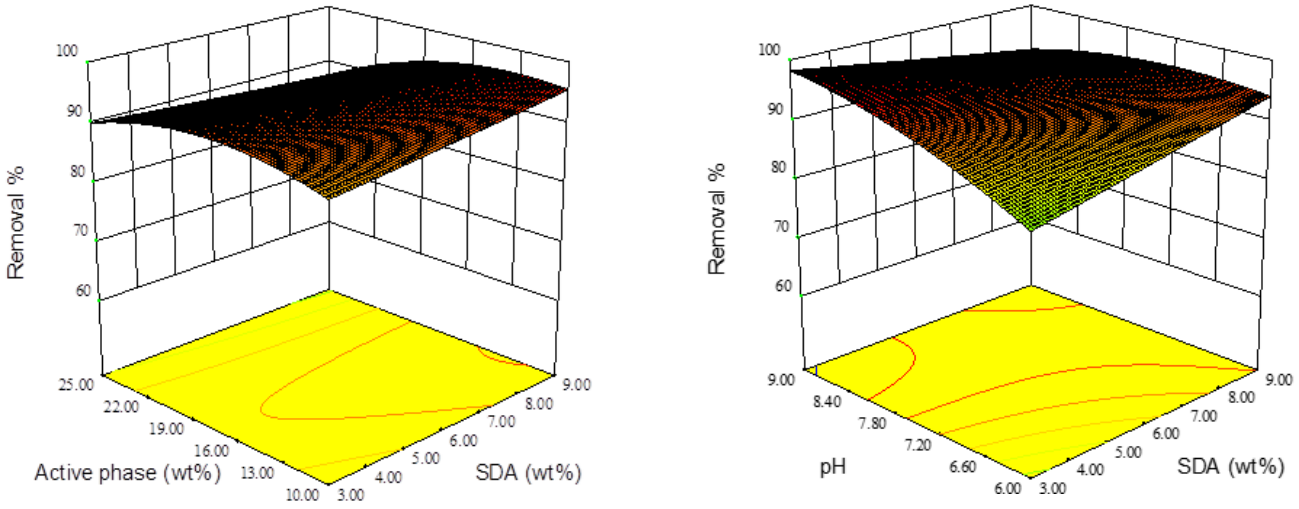

a) Effect of %wt. of gelatine and NiO %wt. **b) Effect of %wt of gelatine and pH of alumina sol.**

Figure 13: 3-D diagram of the effect of synthesis parameters on the removal efficiency of DBT in the ODS. Reaction condition: temperature 60˚C, time 60 minutes, catalyst 0.2g, fuel 50 ml and DBT concentration 500 ppm.

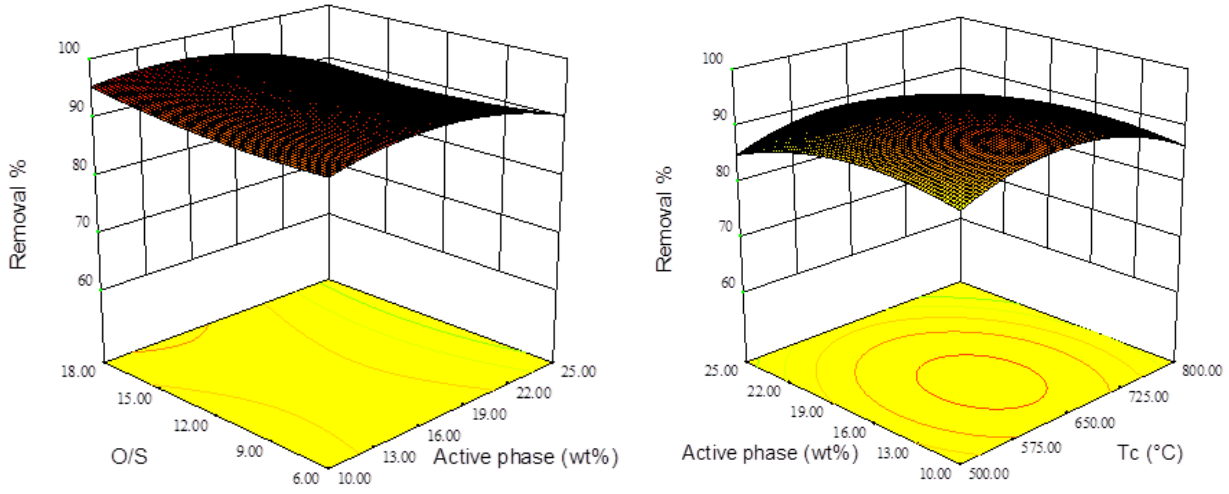

a) Effect of O/S and NiO %wt. **b) Effect of calcination temperatures and NiO %wt.**

Figure 14: 3-D diagram of the effect synthesis parameters on the removal efficiency of DBT in the ODS process. Reaction condition: temperature 60˚C, time 60 minutes, catalyst 0.2g, fuel 50 ml and DBT concentration 500 ppm.

The optimum values for the highest activity of Ni/GeAl$_2$O$_3$(USG) in DBT conversion are listed in Table **1**.

Table 1: The optimal conditions of ODS according to design expert to achieve the maximum DBT removal efficiency, using Ni/GeAl$_2$O$_3$(USG).

Gelatine (% wt.)	pH	Calcination Temperature (˚C)	NiO %wt.	O/S	DBT conversion (%)
3.65	8.7	685	16.86	16.41	98.11

3.5. The Recycling Capability and Stability of the Catalyst

The stability of the optimized Ni/GeAl$_2$O$_3$(USG) catalyst was evaluated through successive DBT desulfurization runs. As shown in Fig. (**15**), DBT conversion gradually decreased from 97.4% to 86.3% over seven cycles, indicating

good catalyst stability. After seven runs, the catalyst was regenerated by washing with methanol for 2 h under stirring, drying at 110 °C for 24 h, and calcining at 500 °C for 5 h. The regenerated catalyst achieved 91.5% DBT removal, confirming effective regeneration.

Sintering of the sub-5 nm γ-Al_2O_3 particles is negligible under these conditions, as they retain their nanoscale size even after calcination at 700 °C, demonstrating excellent thermal stability. Furthermore, the ODS reaction is conducted at 60 °C, well below alumina's Tammann temperature (~900 °C), where significant sintering would occur. Thus, the gradual decline in activity over repeated cycles is primarily attributed to active site poisoning by sulfone by-products [48].

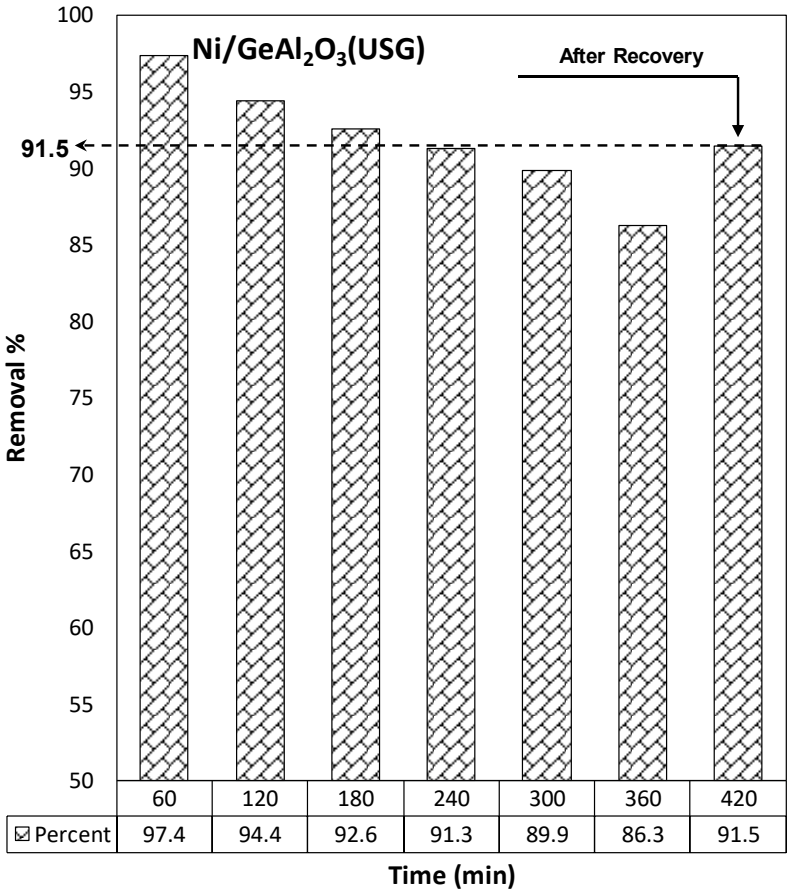

Figure 15: Stability of the catalyst. Reaction condition: temperature 60˚C, time 60 minutes, catalyst 0.2g, fuel 50 ml and DBT concentration 500 ppm.

3.6. Similar Works

As presented in Table **2**, the catalytic performance of NiO supported on bio-synthesized γ-Al_2O_3 catalyst was compared with recently reported catalytic ODS systems. FeMo-O_x/$LaTiO_y$-2 [49] and MoO_3/$LaTiO_x$-2 [50] catalysts achieved complete removal of 4,6-DMDBT at elevated temperature (130 °C) and under continuous oxygen flow conditions, requiring 75 and 150 min, respectively. Similarly, phosphomolybdenum vanadium pyridine ionic liquid systems required prolonged reaction time (8 h) and relatively high temperature (110 °C), while achieving only 65% sulfur removal [51]. Although phosphotungstic acid-UiO-66 exhibited rapid DBT removal (5 min) at room temperature, the system employed a specific oxidant-to-sulfur ratio and extraction conditions that may limit large-scale applicability [52]. In contrast, the NiO-bio-synthesized γ-Al_2O_3 catalyst developed in this work achieved 98.11% DBT removal at a relatively mild temperature (60 °C) within 60 min, without the need for high oxygen flow rates or harsh reaction conditions. These results demonstrate that the present catalyst offers a favorable balance between efficiency, operational simplicity, and moderate reaction conditions, highlighting its potential for practical oxidative desulfurization applications.

Table 2: Comparison with recent catalysts in ODS.

Catalyst	Sulfuric Pollutant	Conditions	Removal Efficiency (%)	Time (min)	Ref.
FeMoOx/LaTiOy-2	4,6-DMDBT	t = 130 °C, stirring speed = 800 r/min, O2 flow rate = 200 cm3 /min	100	75	[49]
MoO3/LaTiOx-2	4,6-DMDBT	130 °C, 20 mg catalyst dosage, and 200 mL/min oxygen flow rate	100	150	[50]
phosphomolybdenum vanadium pyridine ionic liquid	high-sulfur petroleum coke	110 °C, reaction time of 8 h, catalyst dosage of 0.20 g, and air flow rate of 100 mL/min, phosphomolybdenum vanadium pyridine ionic liquid as solvent	65	480	[51]
phosphotungstic acid-UiO-66	DBT	m(model oil) = 2 g, m(MeCN) = 0.3 mL, O/S = 2, m(catalyst) = 30 mg, t = 5 min, T = RT	100	5	[52]
NiO-Bio synthesized γ-Alumina	DBT	60˚C, 60 minutes, catalyst 0.2g, fuel 50ml and DBT concentration 500ppm	98.11	60	This work

4. Conclusions

In this study, four bio-templates—Pistacia Atlantica gum, glucose, gelatine, and gond katira gum—were evaluated for the synthesis of γ-alumina powder. All templates produced γ-alumina, but the gelatine-derived sample exhibited the highest crystallinity and surface area. MoO_3 and NiO were subsequently impregnated on this alumina, with NiO showing superior DBT conversion due to higher surface area and reduced particle agglomeration. NiO impregnation assisted by sonication further increased DBT conversion, attributed to enhanced NiO dispersion and stronger interactions between the active phase and support. Optimization of structural parameters (alumina sol pH, gelatine content, NiO content, calcination temperature) and the operational O/S ratio led to a catalyst achieving 98.11% DBT conversion.

Conflict of Interest

The authors declare that they have no conflicts of interest relevant to the content of this manuscript.

Funding

This research received no specific grant from any funding agency in the public, commercial, or not-for-profit sectors.

References

[1] Boahene PE, Vedachalam S, Dalai AK. Catalytic oxidative desulfurization of light gas oil over Keggin-type phosphomolybdic acid supported on TUD-1 metallosilicates. Fuel. 2022; 317: 123447. https://doi.org/10.1016/j.fuel.2022.123447

[2] Liu D, Quek X-Y, Hu S, Li L, Lim HM, Yang Y. Mesostructured TUD-1 supported molybdophosphoric acid (HPMo/TUD-1) catalysts for n-heptane hydroisomerization. Catal Today. 2009; 147: S51-7. https://doi.org/10.1016/j.cattod.2009.07.017

[3] Wang D, Liu N, Zhang J, Zhao X, Zhang W, Zhang M. Oxidative desulfurization using ordered mesoporous silicas as catalysts. J Mol Catal A Chem. 2014; 393: 47-55. https://doi.org/10.1016/j.molcata.2014.05.026

[4] Wang Y, Hua M, Zhou S, Hu D, Liu F, Cheng H, *et al*. Regulating the coordination environment of surface alumina on $NiMo/Al_2O_3$ to enhance ultra-deep hydrodesulfurization of diesel. Appl Catal B Environ Energy. 2024; 357: 124265. https://doi.org/10.1016/j.apcatb.2024.124265

[5] Liu J, Liu Y, Wang Y, Zhang W, Liang S, You F, *et al*. Regulating the electron affinity of $NiMo/Al_2O_3$ to enhance ultra-deep hydrodesulfurization of diesel. Appl Catal B Environ Energy. 2025; 378: 125565. https://doi.org/10.1016/j.apcatb.2025.125565

[6] Zhou S, Pan Y, Wang Y, Liang S, Cheng H, Huang Y, *et al*. Structure-reactivity relationship of Fe-triggered NiMoS active phase for ultradeep hydrodesulfurization of diesel. Chem Eng Sci. 2025; 317: 122071. https://doi.org/10.1016/j.ces.2025.122071

[7] Khodadadi Dizaji A, Mortaheb HR, Mokhtarani B. Complete oxidative desulfurization using graphene oxide-based phosphomolybdic acid catalyst: process optimization by two phase mass balance approach. Chem Eng J. 2018; 335: 362-72. https://doi.org/10.1016/j.cej.2017.10.129

[8] Luo J, Wang C, Liu J, Wei Y, Chao Y, Zou Y, *et al*. High-performance adsorptive desulfurization by ternary hybrid boron carbon nitride aerogel. AIChE J. 2021; 67: e17280. https://doi.org/10.1002/aic.17280

[9] Alwan HH. Oxidative desulfurization of a model fuel using MoO_3 nanoparticles supported on carbon nanotubes catalyst: examine most significance variables, optimization, kinetics and thermodynamics study. S Afr J Chem Eng. 2022; 40: 230-9. https://doi.org/10.1016/j.sajce.2022.03.002

[10] Deng C, Zhu H, Huang Y, Liu H, Liu P, Cui P, *et al*. High temperature oxidizing-resistant magnetic high entropy catalyst for efficient oxidative desulfurization. Catal Today. 2022; 405-406: 66-74. https://doi.org/10.1016/j.cattod.2022.08.002

[11] Li X, Shi J, Wang J, Xi L, Sun R, Zhang F, *et al*. Preparation of $CeVO_4$/BNNS catalyst and its application in oxidation desulfurization of diesel oil. Fuel. 2023; 337: 126875. https://doi.org/10.1016/j.fuel.2022.126875

[12] Choi AES, Roces S, Dugos N, Futalan CM, Lin S-S, Wan M-W. Optimization of ultrasound-assisted oxidative desulfurization of model sulfur compounds using commercial ferrate (VI). J Taiwan Inst Chem Eng. 2014; 45: 2935-42. https://doi.org/10.1016/j.jtice.2014.08.003

[13] Abdulhadi SA, Alwan HH. Oxidative desulfurization of model fuel using a NiO-MoO_3 catalyst supported by activated carbon: optimization study. S Afr J Chem Eng. 2023; 43: 190-6. https://doi.org/10.1016/j.sajce.2022.10.010

[14] Akbari Moghadam S, Mazloom G, Akbari A, Banisharif F. Supported vanadium oxide catalyst over HY-zeolite-alumina composite fabricated by extrusion for oxidative desulfurization of dibenzothiophene. Mol Catal. 2022; 532: 112731. https://doi.org/10.1016/j.mcat.2022.112731

[15] Abedini F, Allahyari S, Rahemi N. One-step oxidative-adsorptive desulfurization of DBT on simulated solar light-driven nano photocatalyst of MoS_2-C_3N_4-BiOBr@MCM-41. Adv Powder Technol. 2022; 33: 103611. https://doi.org/10.1016/j.apt.2022.103611

[16] Ettekali N, Allahyari S, Rahemi N, Abedini F. One-pot oxidative-adsorptive desulfurization of model and real fuel using micro-mesoporous SiO_2 aerogel supported MoO_3. Microporous Mesoporous Mater. 2021; 326: 111376. https://doi.org/10.1016/j.micromeso.2021.111376

[17] Ullah R, Tuzen M. Interactions of Ni/ZnO with alumina support and their influence on deep reactive adsorption desulfurization. J Mol Liq. 2022; 365: 120082. https://doi.org/10.1016/j.molliq.2022.120082

[18] Du Y, Hu J, Jin Y, Liu Y, Pan Q, Wang K, *et al*. Polyethyleneimine-assisted synthesis of ionic liquid-derived Mo-based mesoporous TiO_2 composite with superior oxidative desulfurization activity. J Environ Chem Eng. 2022; 10: 107143. https://doi.org/10.1016/j.jece.2022.107143

[19] Du Y, Zhou L, Liu Z, Lei J, Li J. Ionic liquid-based 3DOM meso/macroporous Mo/TiO_2 materials with superior oxidation desulfurization performance at room temperature. Mater Res Bull. 2020; 126: 110849. https://doi.org/10.1016/j.materresbull.2020.110849

[20] Yu Z, Xun S, Jing M, Chen H, Song W, Chao Y, *et al*. Construction of 3D TiO_2 nanoflower for deep catalytic oxidative desulfurization in diesel: role of oxygen vacancy and Ti^{3+}. J Hazard Mater. 2022; 440: 129859. https://doi.org/10.1016/j.jhazmat.2022.129859

[21] Ghorbani N, Moradi G. Oxidative desulfurization of model and real oil samples using Mo supported on hierarchical alumina-silica: process optimization by Box-Behnken experimental design. Chin J Chem Eng. 2019; 27: 2759-70. https://doi.org/10.1016/j.cjche.2019.01.037

[22] Mohammadzadeh Yengejeh S, Allahyari S, Rahemi N. Efficient oxidative desulfurization of model fuel by visible-light-driven MoS_2-CeO_2/SiO_2-Al_2O_3 nano photocatalyst coating. Process Saf Environ Prot. 2020; 143: 25-35. https://doi.org/10.1016/j.psep.2020.05.042

[23] Jangi F, Rahemi N, Allahyari S. Oxidative desulfurization using nanocomposites of heterogeneous phosphotungstic acid over natural zeolites: optimization by central-composite design. Pet Sci Technol. 2023; 41: 104-22. https://doi.org/10.1080/10916466.2022.2039703

[24] Chu L, Guo J, Huang Z, Yang H, Yang M, Wang G. Excellent catalytic performance over acid-treated MOF-808(Ce) for oxidative desulfurization of dibenzothiophene. Fuel. 2023; 332: 126012. https://doi.org/10.1016/j.fuel.2022.126012

[25] Li J, Yang Z, Hu G, Zhao J. Heteropolyacid supported MOF fibers for oxidative desulfurization of fuel. Chem Eng J. 2020; 388: 124325. https://doi.org/10.1016/j.cej.2020.124325

[26] Ganiyu SA, Alhooshani K, Sulaiman KO, Qamaruddin M, Bakare IA, Tanimu A, *et al*. Influence of aluminium impregnation on activated carbon for enhanced desulfurization of DBT at ambient temperature: role of surface acidity and textural properties. Chem Eng J. 2016; 303: 489-500. https://doi.org/10.1016/j.cej.2016.06.005

[27] Koopi H, Buazar F. A novel one-pot biosynthesis of pure alpha aluminum oxide nanoparticles using the macroalgae Sargassum ilicifolium: a green marine approach. Ceram Int. 2018; 44: 8940-5. https://doi.org/10.1016/j.ceramint.2018.02.091

[28] Manogar P, Morvinyabesh JE, Ramesh P, Jeyaleela GD, Amalan V, Ajarem JS, *et al*. Biosynthesis and antimicrobial activity of aluminium oxide nanoparticles using Lyngbya majuscula extract. Mater Lett. 2022; 311: 131569. https://doi.org/10.1016/j.matlet.2021.131569

[29] Sifontes ÁB, Ávila E, Gutiérrez B, Rengifo M, Mónaco A, Díaz Y, *et al*. Relevant aspects of the biosynthesis of porous aluminas using glycosides and carbohydrates as biological templates. Biotechnol Res Innov. 2019; 3: 22-37. https://doi.org/10.1016/j.biori.2019.01.004

[30] Filiciotto L, Tosi P, Balu AM, de Jong E, van der Waal JC, Osman SM, *et al*. Humins as bio-based template for the synthesis of alumina foams. Mol Catal. 2022; 526: 112363. https://doi.org/10.1016/j.mcat.2022.112363

[31] Sabu U, Rashad M, Logesh G, Kumar K, Lodhe M, Balasubramanian M. Development of biomorphic alumina using egg shell membrane as bio-template. Ceram Int. 2018; 44: 4615-21. https://doi.org/10.1016/j.ceramint.2017.11.173

[32] Ma Y, Wei Q, Ling R, An F, Mu G, Huang Y. Synthesis of macro-mesoporous alumina with yeast cell as bio-template. Microporous Mesoporous Mater. 2013; 165: 177-84. https://doi.org/10.1016/j.micromeso.2012.08.016

[33] Mohandessi M, Rahimpour MR. Bio-template fabrication of nanoporous Ni@Al_2O_3: durable catalyst for biogas reforming reaction. Ceram Int. 2023; 49(5): 7476-88. https://doi.org/10.1016/j.ceramint.2022.10.217

[34] Lü H, Li P, Deng C, Ren W, Wang S, Liu P, *et al*. Deep catalytic oxidative desulfurization (ODS) of dibenzothiophene (DBT) with oxalate-based deep eutectic solvents (DESs). Chem Commun (Camb). 2015; 51: 10703-6. https://doi.org/10.1039/C5CC03324A

[35] Van Truong T, Kim DJ. Synthesis of high quality boehmite and γ-alumina for phosphorus removal from water works sludge by extraction and hydrothermal treatment. Environ Res. 2022; 212: 113448. https://doi.org/10.1016/j.envres.2022.113448

[36] Zhou Y, Gao Y, Wei S, Pan K, Hu Y. Preparation and characterization of Mo/Al_2O_3 composites. Int J Refract Met Hard Mater. 2016; 54: 186-95. https://doi.org/10.1016/j.ijrmhm.2015.07.033

[37] Mishra YK, Adelung R. ZnO tetrapod materials for functional applications. Mater Today. 2018; 21: 631-51. https://doi.org/10.1016/j.mattod.2017.11.003

[38] Zolghadri S, Honarvar B, Rahimpour MR. Synthesis, application, and characteristics of mesoporous alumina as a support of promoted Ni–Co bimetallic catalysts in steam reforming of methane. Fuel. 2023; 335: 127005. https://doi.org/10.1016/j.fuel.2022.127005

[39] Allahyari S, Haghighi M, Ebadi A, Hosseinzadeh S. Effect of irradiation power and time on ultrasound assisted co-precipitation of nanostructured CuO-ZnO–Al_2O_3 over HZSM-5 used for direct conversion of syngas to DME as a green fuel. Energy Convers Manag. 2014; 83: 212-22. https://doi.org/10.1016/j.enconman.2014.03.071

[40] Allahyari S, Haghighi M, Ebadi A, Hosseinzadeh S. Ultrasound assisted co-precipitation of nanostructured CuO–ZnO–Al_2O_3 over HZSM-5: effect of precursor and irradiation power on nanocatalyst properties and catalytic performance for direct syngas to DME. Ultrason Sonochem. 2014; 21: 663-73. https://doi.org/10.1016/j.ultsonch.2013.09.014

[41] Allahyari S, Haghighi M, Ebadi A, Qavam Saeedi H. Direct synthesis of dimethyl ether as a green fuel from syngas over nanostructured CuO–ZnO–Al_2O_3/HZSM-5 catalyst: influence of irradiation time on nanocatalyst properties and catalytic performance. J Power Sources. 2014; 272: 929-9. https://doi.org/10.1016/j.jpowsour.2014.07.152

[42] Azami M, Haghighi M, Allahyari S. Sono-precipitation of Ag_2CrO_4–C composite enhanced by carbon-based materials (AC, GO, CNT and C_3N_4) and its activity in photocatalytic degradation of acid orange 7 in water. Ultrason Sonochem. 2018; 40: 505-16. https://doi.org/10.1016/j.ultsonch.2017.07.043

[43] Ekka B, Dhaka RS, Patel RK, Dash P. Fluoride removal in waters using ionic liquid-functionalized alumina as a novel adsorbent. J Clean Prod. 2017; 151: 303-18. https://doi.org/10.1016/j.jclepro.2017.03.061

[44] González-Gómez MA, Belderbos S, Yañez-Vilar S, Piñeiro Y, Cleeren F, Bormans G, *et al*. Development of superparamagnetic nanoparticles coated with polyacrylic acid and aluminum hydroxide as an efficient contrast agent for multimodal imaging. Nanomaterials (Basel). 2019; 9: 1626. https://doi.org/10.3390/nano9111626

[45] Maheswari N, Muralidharan G. Controlled synthesis of nanostructured molybdenum oxide electrodes for high performance supercapacitor devices. Appl Surf Sci. 2017; 416. https://doi.org/10.1016/j.apsusc.2017.04.094

[46] Ramanathan A, Castro Villalobos MC, Kwakernaak C, Telalovic S, Hanefeld U. Zr-TUD-1: a Lewis acidic, three-dimensional, mesoporous, zirconium-containing catalyst. Chem Eur J. 2008; 14: 961-72. https://doi.org/10.1002/chem.200700725

[47] Kolar T, Mušič B, Korošec RC, Kokol V. Addition of $Al(OH)_3$ versus AlO(OH) nanoparticles on the optical, thermo-mechanical and heat/oxygen transmission properties of microfibrillated cellulose films. Cellulose. 2021; 28: 9441-60. https://doi.org/10.1007/s10570-021-04129-6

[48] Asadi F, Allahyari S, Rahemi N, Hussain M. One-pot oxidative-adsorptive desulfurization of model fuel and fuel oil using magnetic boron nitride-based catalysts under ultrasonic irradiations. J Ind Eng Chem. 2024; 133: 439-53. https://doi.org/10.1016/j.jiec.2023.12.020

[49] Zhang F, Yan Y, Liu F, Wu Y, Liang S, Cheng H, *et al*. Regulating the Fe/Mo ratio of $FeMoO_x$/$LaTiO_Y$ to boost aerobic oxidative desulfurization of diesel. J Fuel Chem Technol. 2025; 53: 1255-68. https://doi.org/10.1016/S1872-5813(25)60576-7

[50] Cheng H, Wu Y, Shao S, Liang S, You F, Wu H, *et al*. Regulating the metal-support interaction of MoO_3/$LaTiO_x$ to enhance ultra-deep aerobic oxidative desulfurization of diesel. Chem Eng J. 2025; 519: 165375. https://doi.org/10.1016/j.cej.2025.165375

[51] Wang Y, Luan H, Gong J, Hua M, Wu P, Cheng H, *et al*. Mechanochemical driven oxidative desulfurization of high-sulfur petroleum coke over [Bpy]$PMoV_n$ coupled with amide-based binary deep eutectic solvents. Chem Eng Sci. 2025; 304: 121021. https://doi.org/10.1016/j.ces.2024.121021

[52] Lin M, Lou H, Qi Z, Chen J, Ye C, Qiu T. D-alanine-bridged phosphotungstic acid/UiO-66 hybrids as efficient catalysts for oxidative desulfurization of fuels. Chem Eng Sci. 2026; 326: 123545. https://doi.org/10.1016/j.ces.2026.123545